Breaking the Space Charge Limit in Organic Solar Cells by a Novel Plasmonic-Electrical Concept

Wei E.I. Sha, Xuanhua Li, Wallace C.H. Choy*
Department of Electrical and Electronic Engineering, the University of Hong Kong, Pokfulam Road, Hong Kong
Email: chchoy@eee.hku.hk (W.C.H. Choy)

Supporting Information

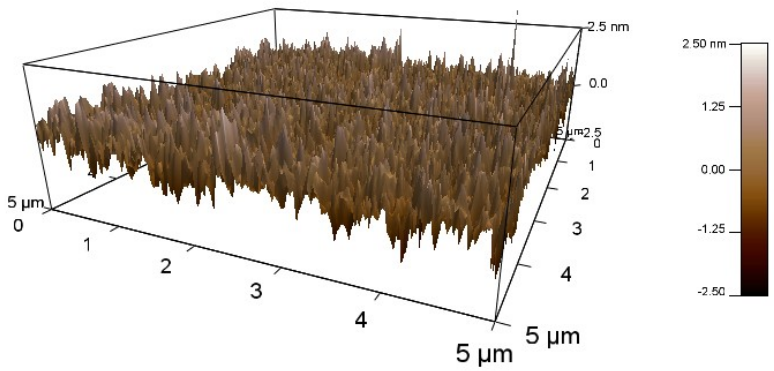

(a)

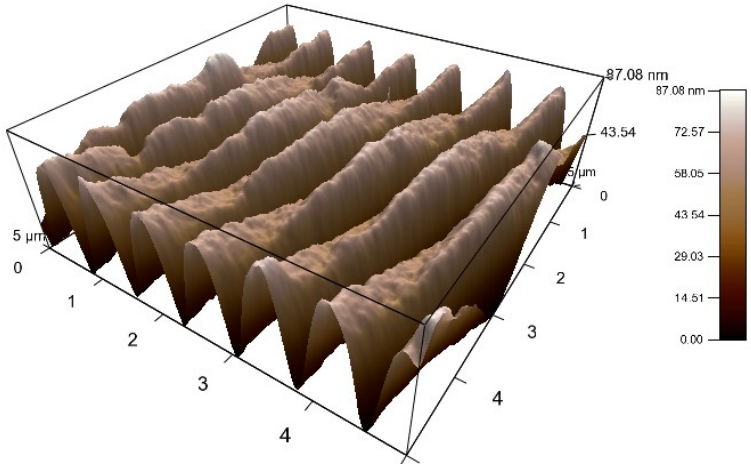

(b)

Supplementary Figure S1. Atomic force microscopy (AFM) images of the P3HT: PCBM film after (a) planar PDMS and (b) grating PDMS mold applied by using nanoimprinted method.

Supplementary Note 1: mobility of holes and electrons. We measure photocarrier (electron and hole) mobility of organic active materials using the space charge limited current (SCLC) model. The hole-dominated device with a structure of ITO/ PEDOT:PSS (30 nm)/ active layer (220 nm)/ MoO_3 (10 nm)/ Ag or Au (100 nm) and the electron-dominated device with a structure of ITO/ TiO_2 (20 nm)/ active layer (220 nm)/ Ca (10 nm)/ Al (100 nm) are employed respectively for measuring the electron and hole mobility at various temperatures T as shown in **Figures S2** and **S3**. It is

observed that at room temperature the electron mobility in the PCBM phase (μ_e=3.44×10^{-4} m^2/Vs) is 125 times larger than the hole mobility in the P3HT phase (μ_h=1.89×10^{-6} m^2/Vs), which are strongly unbalanced. The low hole mobility originates from a hopping process between localized sites in conjugated polymer chain segments. As the temperature decreases, the difference between μ_e and μ_h becomes larger and larger. For example, at 178 K the difference between μ_e and μ_h increases to a factor of 2000, thereby strongly unbalanced transport in these blends is expected.

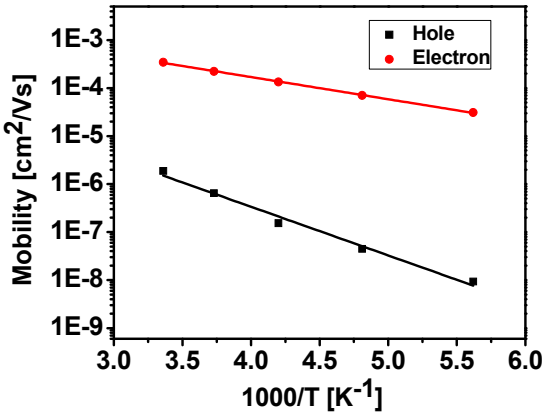

Supplementary Figure S2. Experimental mobility of electrons (μ_e) and holes (μ_h) as a function of inverse temperature (1/T).

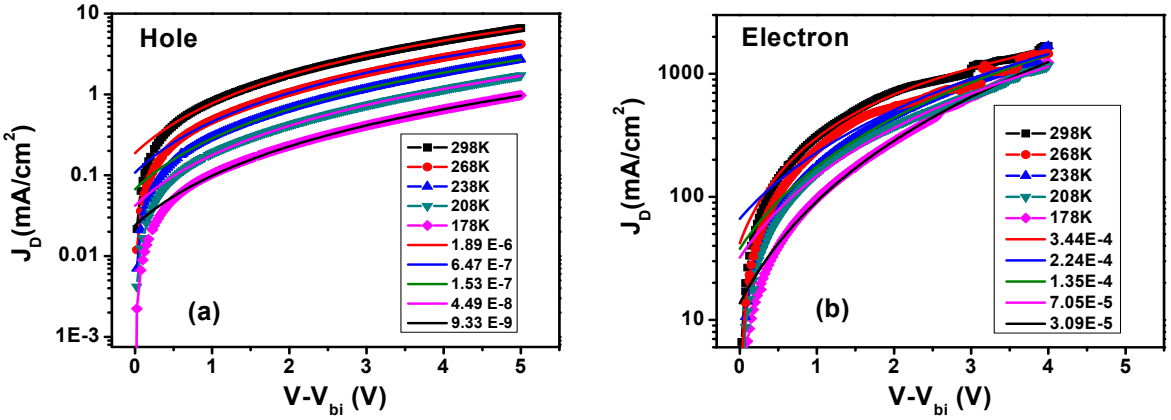

Supplementary Figure S3. (a) The *J-V* characteristics of the hole-only device with a structure of ITO/ PEDOT:PSS (30 nm)/ P3HT:PCBM (220 nm)/ MoO_3 (10 nm)/ Ag or Au (100 nm) at different temperatures. (b) The *J-V* characteristics of the electron-only device with a structure of ITO/ TiO_2 (20 nm)/ P3HT:PCBM (220 nm)/ Ca (10 nm)/ Al (100 nm) at different temperatures.

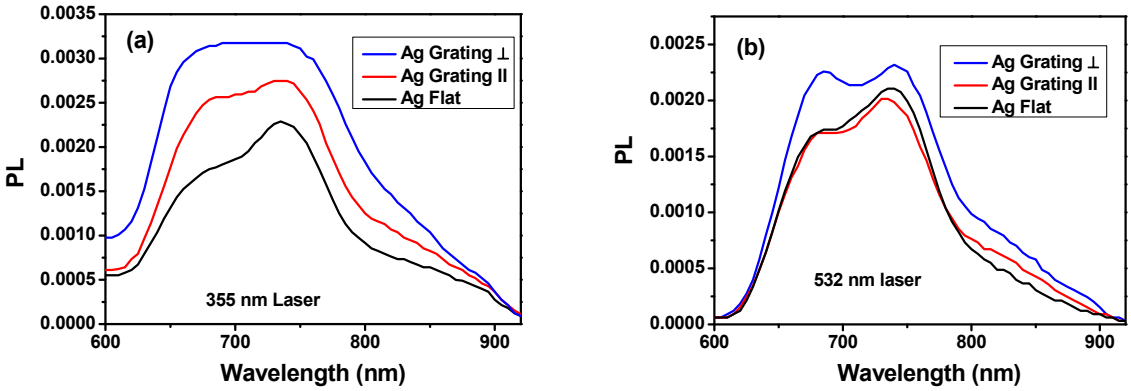

Supplementary Figure S4. PL spectra of the Ag-planar-inverted and Ag-grating-inverted OSCs. "//" means the incident light with a polarization parallel to the grating pitch direction, and "⊥" means the incident light with a polarization perpendicular to the grating pitch direction. (a) 355 nm laser; (b) 532 nm laser.

Supplementary Note 2: photoluminescence. We performed PL measurements to investigate the influence of the Ag grating on exciton generation. **Figure S4** presents the room-temperature PL spectra obtained using polarized laser source (355 and 532 nm) for the Ag-planar-inverted and Ag-grating-inverted devices. It is well known that surface plasmons can only be excited by the incident light with a polarization perpendicular to the grating pitch direction. In order to confirm the absorption enhancement is indeed due to surface plasmons, the Ag-grating-inverted device is excited again with the light polarized parallel to the grating pitch direction, which shows much smaller PL intensity and thus low exciton generation. Consequently, the PL results suggest that excited SPs significantly increase the exciton generation.

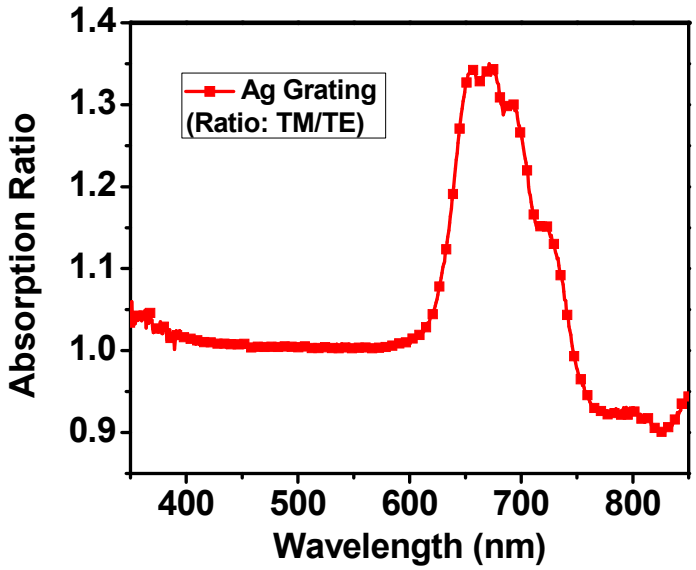

Supplementary Figure S5. The absorption ratio of Ag-grating devices for TE (*s*) and TM (*p*) polarized incident light.

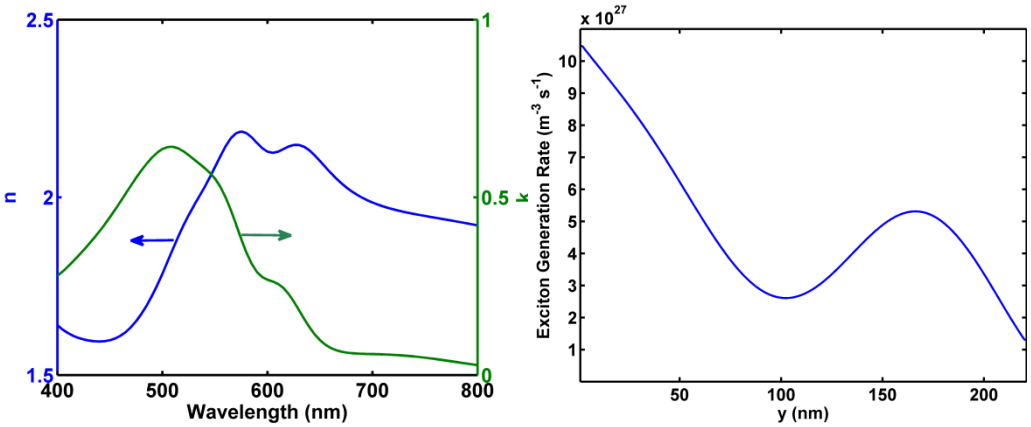

(a) **(b)**

Supplementary Figure S6. (a) Measured complex refractive index of the active material P3HT:PCBM; (b) Theoretical exciton generation distribution in the Ag-planar-inverted OSC.

Supplementary Note 3: theoretical modeling of exciton generation. We employed the finite-difference frequency domain method [Opt. Express, 18(6), 5993-6007, 2010] to calculate the exciton generation for both the planar and grating OSCs. The perfectly matched layer absorbing boundary conditions are used at the top and bottom boundaries of the devices. Using the Bloch-Floquet theorem, the periodic boundary conditions are adopted at the left and right boundaries. The interfaces between different materials are treated by the one-sided difference strategy and averaged material model [Opt. Express, 18(6), 5993-6007, 2010]. The complex permittivity of metals (Ag, Au, etc) can be expressed by the Brendel–Bormann model [Appl. Opt. 37(22), 5271-5283, 1998]. The complex refractive index of the active material P3HT:PCBM are measured by ellipsometry as shown in **Figure S6(a)**. The exciton generation rate can be evaluated by

$$G(\mathbf{r}) = \int_{400}^{800} \frac{2\pi}{h} \varepsilon_0 n(\lambda) k(\lambda) |\mathbf{E}(\mathbf{r},\lambda)|^2 \Gamma(\lambda) d\lambda$$

where n and k are the measured real and imaginary parts of refractive indices of active materials, h is the plank constant, and Γ is the AM 1.5G solar spectrum. **Figure S6(b)** shows the exciton generation distribution for the Ag-planar-inverted OSC with the active layer thickness of 220 nm.

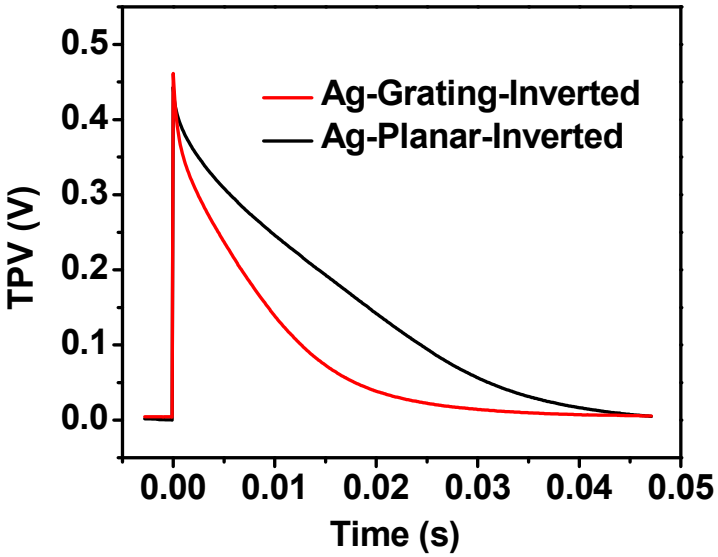

Supplementary Figure S7. Transient photovoltage (TPV) measurements for the Ag-planar-inverted and Ag-grating-inverted OSCs.

Supplementary Note 4: transient photovoltage results. From transient photovoltage (TPV) measurements, we investigated the photocarrier collection which is useful in understanding the SCL characteristics. The TPV measurements using an excitation source of 532 nm picosecond laser pulse show that the transient voltage of the Ag-grating-inverted device decays faster than that of the Ag-planar-inverted device as shown in **Figure S7.** This indicates that low-mobility holes will be collected faster by the Ag-grating anode than by the Ag-planar anode.

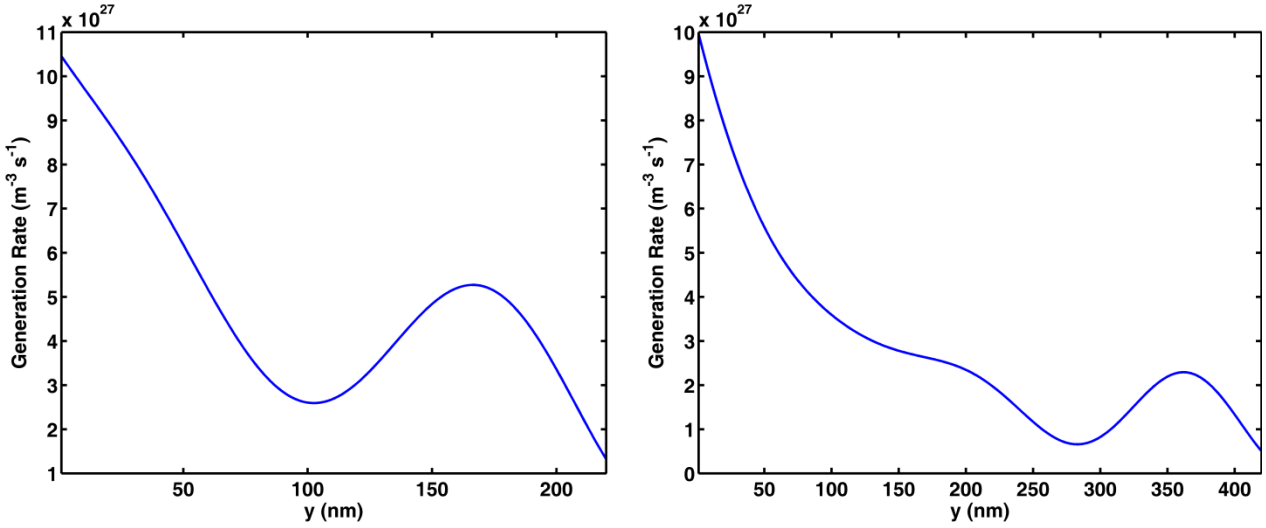

(a) **(b)**

Supplementary Figure S8. Theoretical exciton generation at the active layer of Ag-planar-inverted OSCs. (a) active layer thickness is 220 nm; (b) active layer thickness is 420 nm.

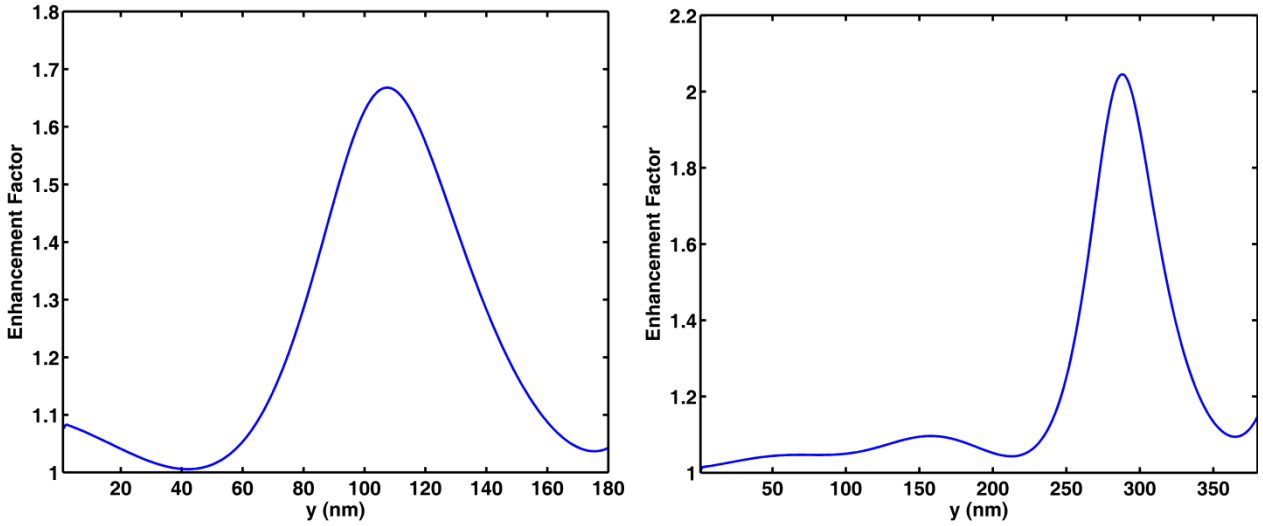

Supplementary Figure S9. Theoretical integrated exciton generation of Ag-grating-inverted OSCs (sinusoidal grating) over that of Ag-planar-inverted ones as shown in **Figure S8**. The integrated exciton generation is defined as $\bar{G}(y)=\frac{1}{P}\int_0^P G(x,y)dx$, where P is the periodicity. Here we did not show the exciton enhancement factor at the region occupied by the grating anode. (a) active layer thickness is 220 nm; (b) active layer thickness is 420 nm.

Supplementary Note 5: thickness-dependent light absorption and SCL effects. The light absorption of active layer shows thickness-dependent features. From **Figure S8**, most photocarriers are generated around the planar cathode (y=0 nm) as the active layer thickness increases. Due to a long transport path of low-mobility holes, the SCL effect will occur at the Ag-planar-inverted OSC with a thick active layer. **Figures S9** suggests the plasmonically enhanced absorption region is around the grating anode with a width of ~100 nm, which is not dependent on the active layer thickness. The enhancement factor also does not show a significant change. Considering the exciton generation of the planar OSCs (**Figure S8**) and the enhancement factors (**Figures S9**) together, fewer photocarriers are generated around the grating anode if the active layer is too thick. Under this situation, the SCL effect will reoccur for the Ag-grating-inverted OSC. In other words, with a moderate thickness of active layer, plasmonic effects induced by the metallic grating anode could eliminate the SCL effect in the planar-inverted OSC.

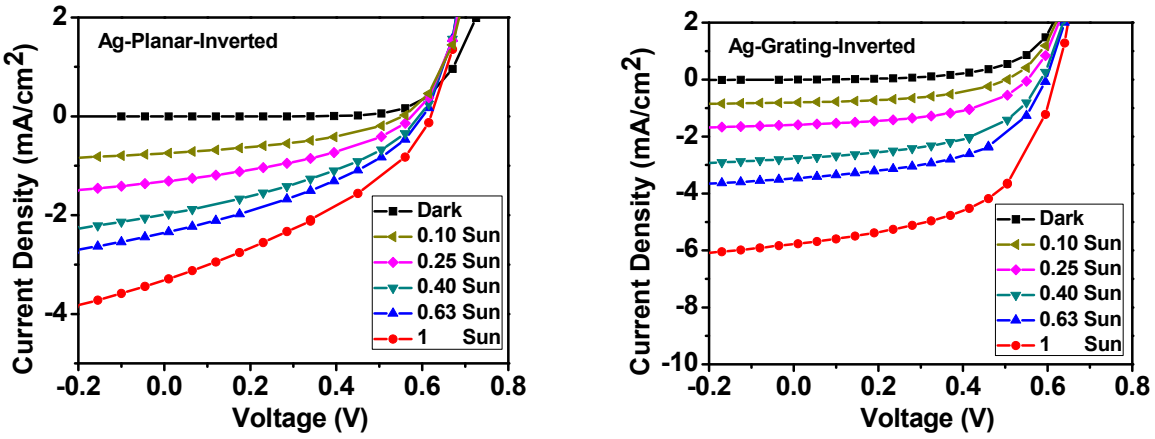

Supplementary Figure S10. Experimental *J-V* curves of the Ag-planar-inverted and Ag-grating-inverted OSCs at different light intensities. The standard AM 1.5G solar spectrum is used in measurements.

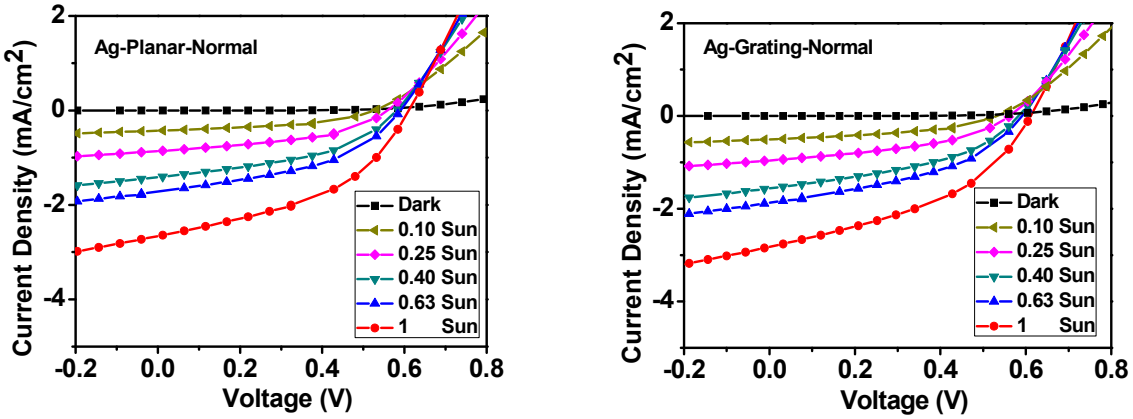

Supplementary Figure S11. Experimental *J-V* curves of the Ag-planar-normal and Ag-grating-normal OSCs at different light intensities. The standard AM 1.5G solar spectrum is used in measurements.

Supplementary Note 6: Figure S12-Figure S14 show experimental results (PL spectra, absorption ratio, and *J-V* curves) for Au-planar and Au-grating OSCs.

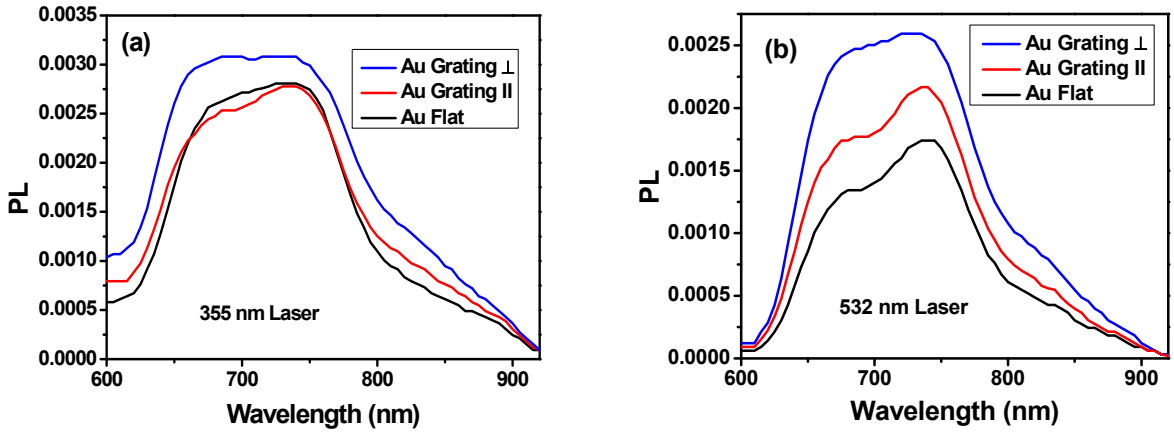

Supplementary Figure S12. PL spectra of the Au-planar-inverted and Au-grating-inverted OSCs. "//" means the incident light with a polarization parallel to the grating pitch direction, and "⊥" means the incident light with a polarization perpendicular to the grating pitch direction. (a) 355 nm laser; (b) 532 nm laser.

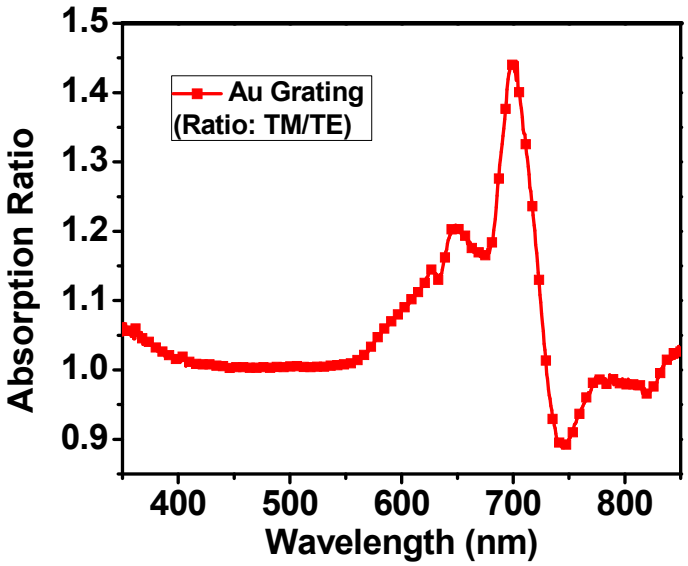

Supplementary Figure S13. The absorption ratio of Au-grating devices for TE (*s*) and TM (*p*) polarized incident light.

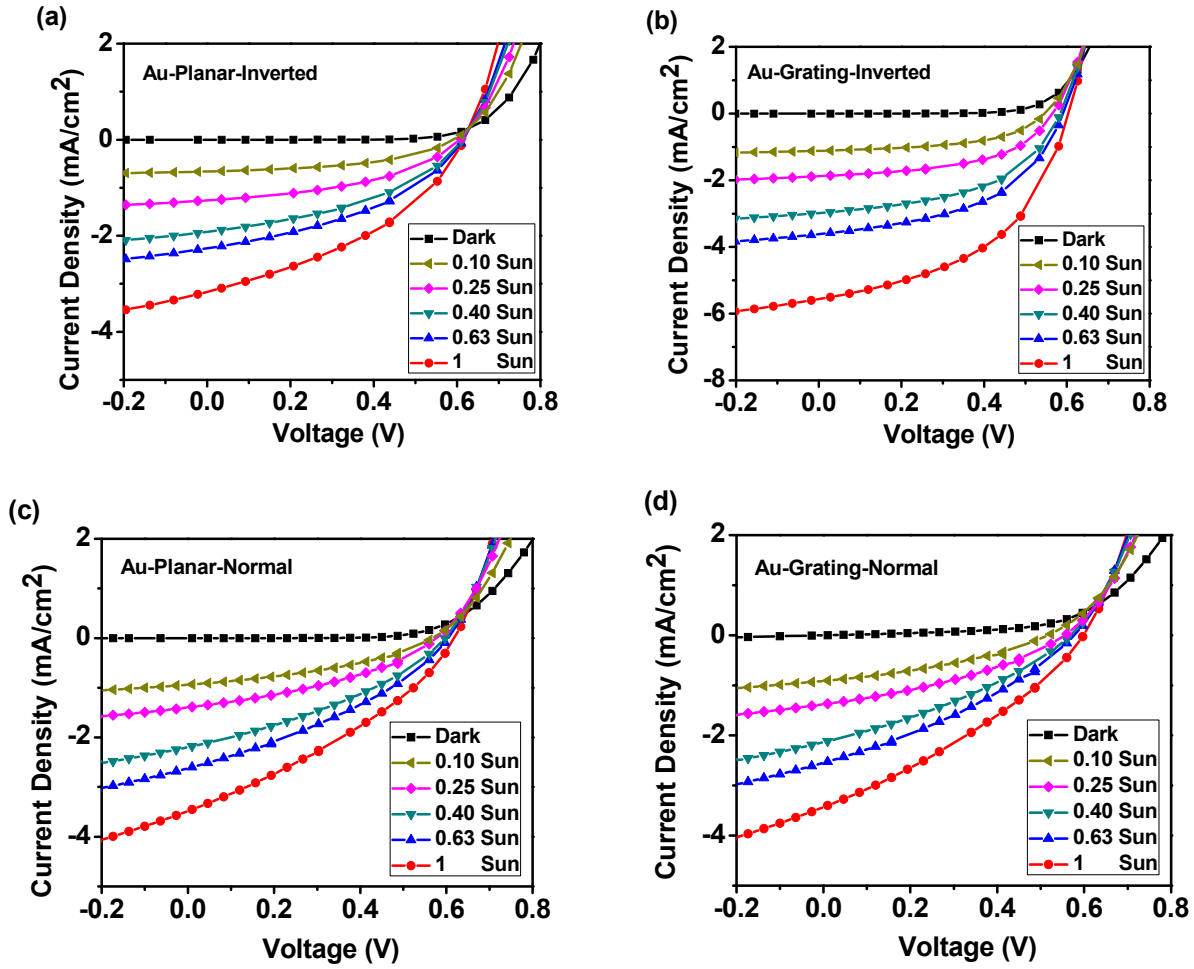

Supplementary Figure S14. Experimental *J-V* curves at different light intensities. The standard AM 1.5G solar spectrum is used in measurements. (a,b) Au-planar-inverted and Au-grating-inverted OSCs; (c,d) Au-planar-normal and Au-grating-normal OSCs.